Biomech Model Mechanobiol (2012) 11:815–827
DOI 10.1007/s10237-011-0354-7

ORIGINAL PAPER

Effect of bending rigidity in a dynamic model of a polyurethane prosthetic mitral valve

X. Y. Luo · B. E. Griffith · X. S. Ma · M. Yin · T. J. Wang · C. L. Liang · P. N. Watton · G. M. Bernacca

Received: 1 March 2011 / Accepted: 7 October 2011 / Published online: 26 October 2011

Abstract We investigate the behaviour of a dynamic fluid–structure interaction model of a chorded polyurethane mitral valve prosthesis, focusing on the effects on valve dynamics of including descriptions of the bending stiffnesses of the valve leaflets and artificial chordae tendineae. Each of the chordae is attached at one end to the valve annulus and at the other to one of two chordal attachment points. These attachment points correspond to the positions where the chords of the real prosthesis would attach to the left-ventricular wall, although in the present study, these attachment points are kept fixed in space to facilitate comparison between our simulations and earlier results obtained from an experimental test rig. In our simulations, a time-dependent pressure difference derived from experimental measurements drives flow through the model valve during diastole and provides a realistic pressure load during systole. In previous modelling studies of this valve prosthesis, the valve presents an unrealistically large orifice at beginning of diastole and does not close completely at the end of diastole. We show that including a description of the chordal bending stiffness enables the model valve to close properly at the end of the diastolic phase of the cardiac cycle. Valve over-opening is eliminated only by incorporating a description of the bending stiffnesses of the valve leaflets into the model. Thus, bending stiffness plays a significant role in the dynamic behaviour of the polyurethane mitral valve prosthesis.

Keywords Mitral valve · Immersed boundary methods · Dynamic simulation · Adaptive method · Chordae tendineae · Bending stiffness · Boundary conditions · Fluid–structure interaction · Polyurethane prosthesis

X. Y. Luo (✉) · X. S. Ma
School of Mathematics and Statistics, University of Glasgow, Glasgow, UK
e-mail: xiaoyu.luo@glasgow.ac.uk

B. E. Griffith
Leon H. Charney Division of Cardiology, Department of Medicine, New York University School of Medicine, New York, NY, USA

M. Yin · T. J. Wang
Department of Engineering Mechanics, Xi'an Jiaotong University, Xi'an, China

C. L. Liang
Department of Mechanical and Aerospace Engineering, George Washington University, Washington, DC, USA

P. N. Watton
Institute of Biomedical Engineering, Department of Engineering Science, University of Oxford, Oxford, UK

G. M. Bernacca
Division of Cardiovascular and Medical Sciences, Gardiner Institute, University of Glasgow, Glasgow, UK

1 Introduction

Heart disease is the major cause of death in the developed world, with valvular heart disease being one of the main disorders. It is known, for instance, that the remodelling that occurs after a posterolateral myocardial infarction can alter mitral valve function by creating conformational abnormalities in the mitral annulus and in the posteromedial papillary muscle, leading to mitral regurgitation and ultimately requiring valve repair or replacement (Einstein et al. 2010). Each year, approximately 250,000 valve replacement procedures are carried out worldwide (Yoganathan et al. 2004). Prosthetic heart valves may be mechanical or bioprosthetic. Mechanical valves are quite durable, but they can induce thrombosis, and their use therefore necessitates sustained anticoagulation therapy. Bioprostheses are less

prone to thrombogenesis but generally fail 10–15 years post-implantation because of structural degradation. An ideal valve replacement would produce a low flow resistance, yield a small regurgitant volume, minimise turbulence, induce low shear stresses, and avoid stagnation and flow separation (Yoganathan et al. 2005). More than 50 types of prosthetic valves have been developed since 1950 (Vongpatanasin et al. 1996). Yet, six decades later, we still use devices that are less than satisfactory. Understanding valve mechanics using computational modelling represents an important step towards improved valve designs and could lead to better diagnosis, treatment and prevention of valvular heart diseases.

Although there have been numerous studies on modelling heart valves, the mitral valve has been much less extensively studied in comparison to the aortic valve, presumably because of the complex structure of the mitral valve and its stronger interaction with blood flow and ventricular motion. Recently, however, there has been increased interest in computational models of mitral valves, and the sophistication of these models has increased in concert with the development of numerical methods and imaging modalities. Kunzelman et al. were the first to use a three-dimensional computational approach to simulate normal mitral function (Kunzelman et al. 1993; Einstein et al. 2003, 2005), the biomechanics underlying valvular disease (Kunzelman et al. 1997, 1998a,b), and surgical interventions (Reimink et al. 1996; Kunzelman et al. 1998a,b). Three-dimensional dynamic modelling of the ovine mitral valve has also been performed by Lim et al. (2005), who focused on the asymmetric stress pattern of the mitral valve. Prot et al. reported their work on mitral valve simulations in a series of studies using a transversely isotropic strain-energy functional with the nonlinear finite element (FE) code ABAQUS (Prot et al. 2007, 2009, 2010; Prot and Skallerud 2009). Recently, their model has been applied to predict the mechanical difference between the healthy mitral valve and the valve in a hypertrophic obstructive cardiomyopathic heart (Prot et al. 2010) and active muscle contraction (Skallerud et al. 2011). Kim et al. (Kim et al. 2007, 2008; Kim 2009) carried out dynamic simulations of a pericardial bioprosthetic heart valve based on a FE shell model, although their primary focus is on the aortic valve. Maisano et al. (2005) and Votta et al. (2007, 2008) used patient-specific FE models to analyse the effects of annuloplasty procedures. The biomechanical response of the valve to the Alfieri stitch technique was reported by Dal Pan et al. (2005) and Votta et al. (2008). The effects of the annular contraction on mitral valve stress were modelled by Stevanella et al. (2009). Urankar (2008) used the LS-DYNA code to model mitral valve fibre stress under various loading and surgical conditions.

Kaazempur–Mofrad and Weinberg used FE shell models and fully three-dimensional FE models to predict the dynamic behaviour of the mitral valve (Weinberg 2005). Their work incorporated fibre direction as an additional degree of freedom to model the large-deformation and anisotropic behaviour of mitral valves, and their method was demonstrated using an existing constitutive law for mitral valve tissue (Weinberg and Kaazempur-Mofrad 2007). Wenk et al. (2010) developed a FE model of the left ventricle, mitral apparatus and chordae tendineae from magnetic resonance (MR) images obtained from sheep. Krishnamurthy et al. (2009) used inverse FE analysis and radiopaque markers sewn to the mitral annulus to show that, unlike isolated leaflets, the in vivo elastic response of the anterior mitral leaflet is linear over a physiologic range of pressures. Arnoldi et al. (2010) developed mitral valve model-construction software with a graphical user interface (GUI), in which they integrated FE computations with four-dimensional echocardiographic image processing in a high-performance computing (HPC) environment. They found this approach to accelerate the process of mitral valve modelling for patient-specific analysis. There are also several recent review papers on mitral valve research, each with a different focus (Sacks et al. 2009; Einstein et al. 2010; Weinberg et al. 2010).

In contrast to the above approaches, in which native human or animal valves are of primary interest, our group has developed a sequence of fully three-dimensional fluid–structure interaction models of a polyurethane prosthetic mitral valve (Watton et al. 2007, 2008; Griffith et al. 2009; Yin et al. 2010). In these studies, the dynamic behaviour of a three-dimensional chorded mitral prosthesis is modelled using the immersed boundary (IB) method, which accounts for the fluid–structure interaction between the blood flow and the mitral valve leaflets. A major limitation of these earlier models is that, with the exception of Griffith et al. (2009), they employed a first-order accurate IB method that resulted in excessive numerical dissipation.

In the present paper, we also model the prosthetic mitral valve using a formally second-order accurate (Lai and Peskin 2000; Griffith and Peskin 2005) version of the IB method. We first verify a cell-centred version of the IB methodology by simulating the flow within a collapsible channel. The results produced by the IB scheme are shown to be in excellent quantitative agreement with results from a well-tested in-house arbitrary Lagrangian–Eulerian (ALE) code (Luo et al. 2008). We then use a staggered-grid IB method to model the dynamics of the prosthetic mitral valve. Unlike our previous work, in which the flow rate is specified at the inlet (Watton et al. 2007, 2008; Griffith et al. 2009), herein, we use pressure boundary conditions at both the inlet and outlet, allowing us to impose a pressure difference across the model valve that is derived from experimental pressure measurements. The imposed pressure difference drives flow through the model valve during the diastolic phase of the cardiac cycle and provides a realistic pressure load for the closed valve during the systolic phase of the cardiac cycle and thereby enables us to perform

more realistic simulations. Using this fluid–structure interaction model of the valve prosthesis, we consider the effects on the dynamics of the valve of including models of the bending rigidity of the chordae and of the leaflets. We demonstrate that when both effects are included in our model, our computational results agree well with experimental measurements. Our simulations therefore indicate that incorporating a model of the bending stiffness is highly important, even for structures as thin as mitral valve leaflets. Although we only present results using IB models of heart valve dynamics, we expect that our findings would also hold for other approaches to modelling the fluid dynamics of heart valves.

2 The immersed boundary (IB) method

2.1 Mathematical formulation

We briefly introduce the immersed boundary (IB) formulation of problems in which an elastic structure is immersed in a viscous incompressible fluid. This formulation uses a Lagrangian description of the elasticity of the structure and an Eulerian description of the momentum, viscosity and incompressibility of the coupled fluid-structure system. Let $x = (x_1, x_2, x_3) \in \Omega$ denote Cartesian (physical) coordinates, in which $\Omega \subset \mathbb{R}^3$ is the physical domain; let $\mathbf{s} = (r, s) \in U$ denote Lagrangian (material) coordinates attached to the structure, in which $U \subset \mathbb{R}^2$ is the Lagrangian coordinate domain; and let $\mathbf{X}(\mathbf{s}, t) \in \Omega$ denote the physical position of material point $\mathbf{s}$ at time t. The IB formulation of the equations of motion for the coupled fluid-structure system is as follows:

$$\begin{aligned}
&\rho\left[\frac{\partial \mathbf{u}}{\partial t}(\mathbf{x},t) + \mathbf{u}(\mathbf{x},t)\cdot\nabla\mathbf{u}(\mathbf{x},t)\right] \\
&\quad = -\nabla p(\mathbf{x},t) + \mu\nabla^2\mathbf{u}(\mathbf{x},t) + \mathbf{f}(\mathbf{x},t), \\
&\nabla\cdot\mathbf{u}(\mathbf{x},t) = 0, \\
&\frac{\partial \mathbf{X}}{\partial t}(\mathbf{s},t) = \int_\Omega \mathbf{u}(\mathbf{x},t)\delta(\mathbf{x}-\mathbf{X}(\mathbf{s},t))\mathrm{dx}, \\
&\mathbf{f}(\mathbf{x},t) = \int_U \mathbf{F}(\mathbf{s},t)\delta(\mathbf{x}-\mathbf{X}(\mathbf{s},t))\mathrm{ds}, \qquad (1\text{–}4)
\end{aligned}$$

in which $\mathbf{u}(\mathbf{x}, t)$ is the Eulerian fluid velocity field, $p = (\mathbf{x}, t)$ is the Eulerian pressure field, $\mathbf{f} = (\mathbf{x}, t)$ is the Eulerian elastic force density generated by the immersed structure (i.e. the elastic force density with respect to the physical coordinate system $\mathbf{x} = (x_1, x_2, x_3)$), $\mathbf{F}(\mathbf{s}, t)$ is the Lagrangian elastic force density generated by the immersed structure (i.e. the elastic force density with respect to the material coordinate system $\mathbf{s} = (r, s)$), ρ is the (uniform) fluid density, μ is the (uniform) fluid viscosity and $\delta(\mathbf{x}) = \delta(x_1)\delta(x_2)\delta(x_3)$ is the three-dimensional Dirac delta function. For further discussion of the IB formulation of problems of fluid–structure interaction, see Peskin (2002).

2.2 Numerical discretisation

To approximate Eqs. (1–4), the incompressible Navier–Stokes equations are discretised on a fixed Eulerian grid, and the equations describing the deformation and elasticity of the immersed structure are discretised on a moving Lagrangian mesh that is allowed to cut freely through the background Eulerian grid. Interaction between Lagrangian and Eulerian variables is handled by a regularized approximation to the three-dimensional Dirac delta function, $\delta_h(\mathbf{x}) = \delta_h(x_1)\delta_h(x_2)\delta_h(x_3)$, in which h is the Eulerian grid spacing. Various formulations of the regularized delta function are possible, but in the simulations described in this paper, we use a version of the four-point delta function (Peskin 2002), so that $\delta_h(x) = \frac{1}{h}\varphi\left(\frac{x}{h}\right)$ with

$$\varphi(r) = \frac{1}{8}\begin{cases} 3 - 2|r| + \sqrt{1 + 4|r| - 4r^2}, & \text{if } |r| \le 1, \\ 5 - 2|r| + \sqrt{7 + 12|r| - 4r^2}, & \text{if } 1 \le |r| \le 2, \\ 0, & \text{otherwise.} \end{cases} \qquad (5)$$

This regularized delta function is constructed to ensure that force and torque are conserved during Lagrangian–Eulerian interaction for problems involving periodic or free-space Eulerian boundary conditions and for problems in which the immersed elastic structure does not attach to or interact with exterior physical boundaries in the Eulerian domain (Peskin 2002). In our simulations, however, we use flow chambers that attach directly to the outer boundaries of the Eulerian physical domain, where we impose physical boundary conditions. In the vicinity of such physical boundaries, we instead use the modified four-point delta function of Griffith et al. (2009). This extended approach ensures that force and torque are conserved during Lagrangian–Eulerian interaction even when the elastic structure is attached to physical boundaries in the Eulerian domain.

2.3 Continuous and discrete elasticity modelling

To describe the elasticity of the immersed structure, it is convenient to assume that the structure is described in terms of overlapping families of elastic fibres and that the Lagrangian material coordinates $\mathbf{s} = (r, s)$ have been chosen so that a fixed valve of $r = r^0$ labels a particular fibre. The elastic forces generated by the immersed structure are the sum of the fibre forces due to extension and bending:

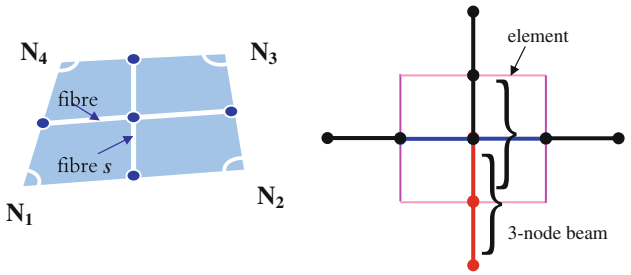

Fig. 1 (*Left*) The 4-node element is spanned by four fibre segments; (*right*) the bending stiffness for a 3-node beam is computed from a pair of adjacent fibre segments located within and across the element boundaries in each direction

$$\mathbf{F} = \mathbf{F}_{\mathrm{s}} + \mathbf{F}_{\mathrm{b}} = \frac{\partial}{\partial s}(T\boldsymbol{\tau}) + \frac{\partial^2}{\partial s^2}\left[k\frac{\partial^2 \mathbf{X}}{\partial s^2}\right], \tag{6}$$

in which $T = T(\mathbf{s})$ is the fibre tension, $\boldsymbol{\tau} = \frac{\partial \mathbf{X}}{\partial s} \Big/ \left|\frac{\partial \mathbf{X}}{\partial s}\right|$ is the unit tangent vector in the fibre direction and k is the bending stiffness coefficient, which is defined as

$$k = EI. \tag{7}$$

In this paper, we use a 4-node quadrilateral element to represent the valve leaflets, see Fig. 1a. Each element is comprised of 8 fibre segments, and the bending stiffness is computed from the 3-node beam element consists of a pair of adjacent fibres, as shown in Fig. 1b. See Watton et al. (2007) for a detailed description of this method for generating elastic fibres from quadratic elements. Note that in Eq. (6), $\mathbf{F}_{\mathrm{s}}$ corresponds to forces generated by extension- and compression-resistant elastic elements, which result in a membrane-type force, and $\mathbf{F}_{\mathrm{b}}$ corresponds to forces generated by bending-resistant elastic elements, which results in a shell-like force. A linear elastic response is assumed, as justified by an earlier comparison between simulation and experiment (Watton et al. 2007).

2.4 Feedback forcing

We provide an additional Eulerian feedback-forcing term to ensure that any Dirichlet boundary conditions are satisfied at the inlet and the outlet. This additional body force, which is nonzero only in the vicinity of the physical boundaries, is of the form

$$\mathbf{f}_{\mathrm{B}}(\mathbf{x}, t) = \kappa(\mathbf{u}_{\mathrm{b}}(\mathbf{x}, t) - \mathbf{u}(\mathbf{x}, t)), \tag{8}$$

in which $\mathbf{u}_{\mathrm{b}}(\mathbf{x}, t)$ is the prescribed velocity along the boundary $\partial\Omega$ of the Eulerian domain. At open boundaries, where we impose normal traction boundary conditions, we employ feedback forcing for only the tangential components of the velocity in the vicinity of $\partial\Omega$. We choose $\kappa = \frac{\rho}{2\Delta t}$, which is approximately the largest value of κ permitted by our semi-implicit time discretisation.

2.5 Implementation

The simulations described herein employ the freely available IBAMR code (http://ibamr.googlecode.com), an adaptive and distributed-memory parallel implementation of the IB method that provides software infrastructure for developing fluid–structure interaction models that use the IB method. IBAMR leverages functionality provided by other freely available software libraries, including SAMRAI (http://computation.llnl.gov/casc/SAMRAI) (Hornung and Kohn 2002; Hornung et al. 2006), PETSc (http://www.mcs.anl.gov/petsc) (Balay et al. 1997, 2008, 2009) and hypre (http://www.llnl.gov/CASC/hypre) (Falgout and Yang 2002).

3 Method verification: collapsible channel flow

3.1 Model description and parameters

In this section, we verify a formally second-order accurate cell-centred IB method (Griffith and Peskin 2005; Griffith 2005; Griffith et al. 2007, 2009) implemented in the IBAMR software framework against an in-house ALE code (Cai and Luo 2003) on a collapsible channel flow problem. This problem is chosen because the rich dynamic behaviour of collapsible channel flows makes simulating fluid–structure interaction in such systems extremely challenging and because, for this particular example, our benchmark ALE code satisfies the geometrical conservation law exactly (Liu et al. 2011). The numerical model consists of flow in a channel in which part of the upper wall is replaced by an elastic beam in the plane strain configuration, see Fig. 2. The rigid channel has width D, and part of the upper wall of length L, scaled by the channel width D, is replaced by an elastic beam that is subject to an external pressure load $\bar{p}_{\mathrm{e}}$. The lengths of the upstream and downstream rigid parts of the channel are L_{u} and L_{d}, respectively, also defined in reference to the channel width D. Steady Poiseuille flow with average velocity U_0 is prescribed as a boundary condition at the inlet. The extensional and bending stiffnesses of the beam are EA and EJ, respectively, in which E is the Young's modulus for the plane strain problem, A is the cross-sectional area of the beam (which is equivalent to the beam's thickness because the beam has unit width in the z direction), and J is the moment of inertia of the cross-section of the beam. Pretension in the beam is assumed to be zero, and the damping and rotational inertia of the beam are ignored. In the ALE code, the beam is discretized using 6-node triangular elements, whereas in the IB simulation, the beam is represented using systems of extension-, compression-, and bending-resistant elastic elements.

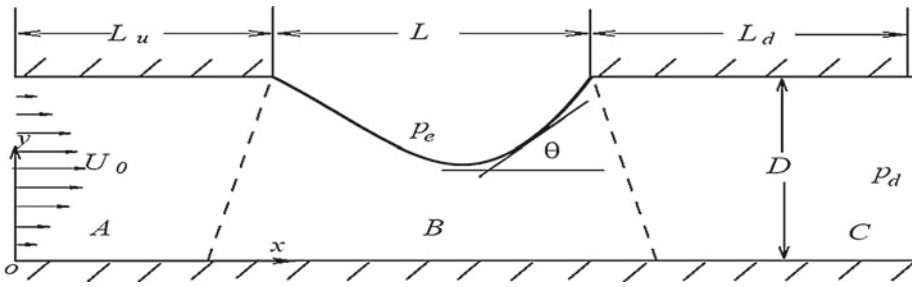

Fig. 2 The configuration of the collapsible channel flow problem (not to scale). In section B, part of the solid upper wall is replaced by an elastic beam. In the IB version of this model, fluid is present both in the interior of the channel and in the space exterior to the channel; in the ALE model, the exterior space is treated as a constant-pressure reservoir

We remark that the physical systems modelled by the IB method and by the ALE code are slightly different. Specifically, the IB model describes a collapsible channel that is immersed in fluid, i.e., a system that includes inertial effects both within the channel and outside of the channel. In contrast, the ALE model excludes inertial effects in the exterior of the channel, thereby effectively treating the region exterior to the channel as a constant-pressure reservoir (Luo et al. 2008). The dynamic behaviour of the two models therefore differs. However, if the system is stable and admits only a single steady solution, then as $t \to \infty$, transient effects will decay, and the equilibrium results of the two models will be identical. Hence, for verification purposes, we consider a stable flow case used by Liu et al. (2009), with dimensionless parameters $c_\lambda = \frac{EA}{\rho U_0^2 D} = 2{,}400$, $Re = \frac{U_0^2 D\rho}{\mu} = 500$, $p_e = \frac{\bar{p}_e}{\rho U_0^2} = 1.95$, $L_u = 5$, $L_d = 30$ and $L = 5$. The corresponding dimensional parameters are $E = 0.4785\,\text{MPa}$, $U_0 = 0.05\,\text{m/s}$, $\rho = 10^3\,\text{kg/m}^3$, $\mu = 10^{-3}\,\text{Pa s}$, $D = 0.01\,\text{m}$, $A = 10^{-4}\,\text{m}^2$ and $\bar{p}_e = 4.875\,\text{Pa}$.

3.2 Results

The undeformed state is used as the initial configuration. Because the wall stiffness is quite large, the largest stable time step for this problem is approximately $5 \times 10^{-5}\,\text{s}$. Figure 3a shows that in the IB model, the wall oscillates for approximately 17 s before settling to a steady state. This quasi-steady solution agrees very well with the results computed from an FE model using our ALE code (Cai and Luo 2003) and also with results obtained using ADINA (Watertown, Massachusetts, United States); see Fig. 3b.

We remark that although steady-state problems, such as the one considered in this section, are well suited for use as verification tests for the IB method, the IB method is primarily intended for simulating dynamic problems, and the performance of the IB method may not be competitive with numerical methods specifically developed for steady-state flow problems. The strength of the IB method, and of its implementation in the IBAMR software, is its ability to enable fully coupled fluid–structure interaction simulations in the dynamic setting for complex three-dimensional geometries, as we demonstrate in the following section.

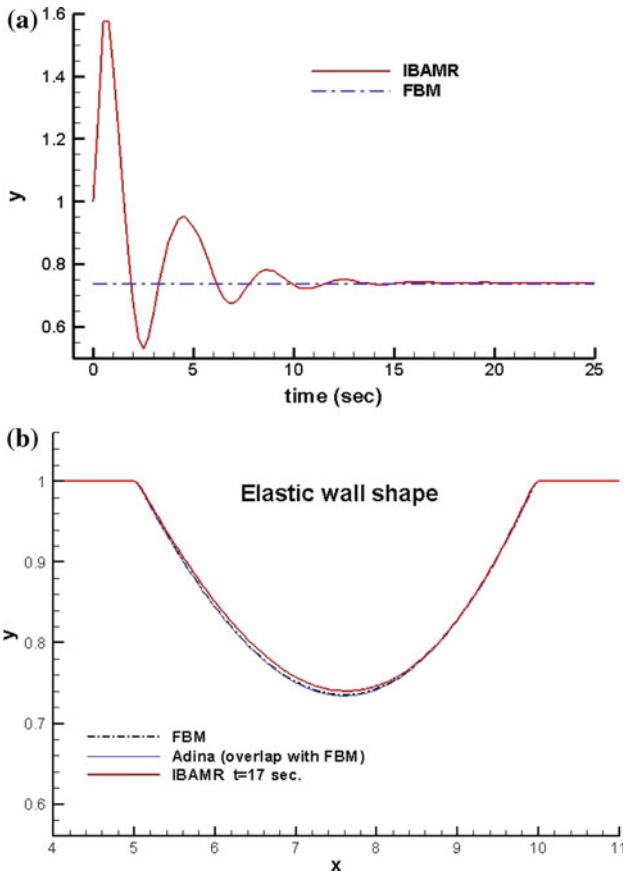

Fig. 3 **a** The y-position of the centre of the elastic beam as a function of time, and **b** the shape of the elastic wall at time $t = 17\,\text{s}$. These results show that the transient solution determined by the IB method implemented in the IBAMR code approaches the steady solution determined by an in-house ALE code (FBM) and also the steady solution determined by ADINA. At equilibrium, all three codes produce results that are in excellent quantitative agreement. In the IB model, the elastic beam is initially flat and aligned with the rigid portions of the upper channel wall (i.e. with $y = 1$). The equilibrium shape shown in panel (**b**) therefore represents a large deformation from this initial configuration

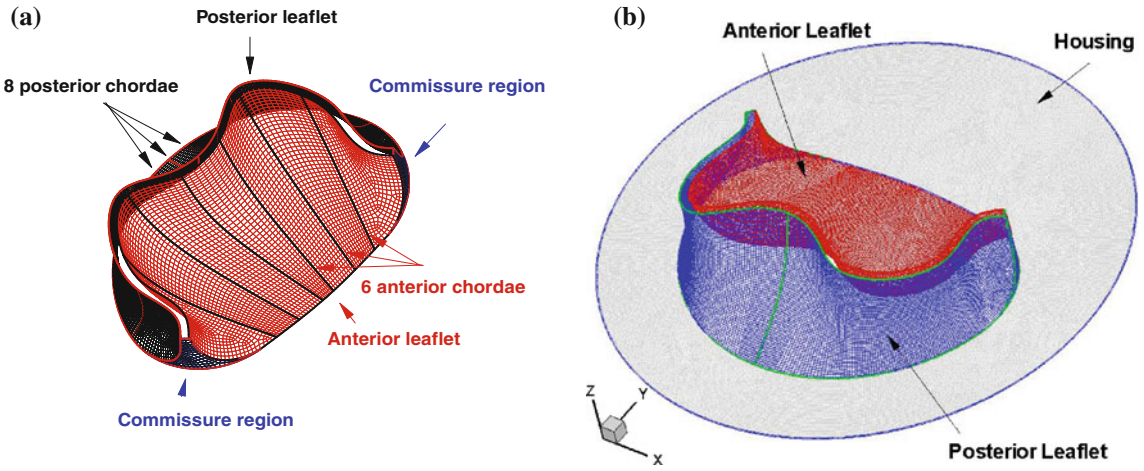

Fig. 4 **a** The mitral valve mesh, and **b** the mitral valve mounted on a rigid housing disc. The anterior leaflet has 22,328 fibre segments, the posterior leaflet has 25,614 fibre segments and the housing disc has 43,404 fibre segments

4 Dynamic simulation of the mitral valve prosthesis

4.1 Model description and parameters

The mitral valve prosthesis that we model is the same as that considered by Watton et al. (2007, 2008) and by Griffith et al. (2009) and is shown in Fig. 4. The valve prosthesis is made of the polyurethane material PurSpan (DSM Biomedical, Berkeley, California, United States) and incorporates artificial chordae tendineae made of Bionate 750D that originate from the valve annulus and traverse each leaflet before exiting at the free margins of the leaflet to attach to the papillary muscle regions of the left-ventricular wall. The prosthetic valve has a total of 14 artificial chordae, with eight in the posterior leaflet and six in the anterior leaflet. The valve is mounted on a rigid D-shaped annulus that attaches to the left ventricle, see Fig. 5. The geometry of the model mitral valve is generated using the SolidWorks CAD software (Concord, Massachusetts, United States). For the purposes of the IB simulation, the model valve is further discretised as a surface that is spanned by overlapping collections of one-dimensional fibre segments, see Fig. 1.

Each of the chordae has a cross-sectional area of 0.4 mm^2 and a Young's modulus of 30 MPa. The leaflets have a mean thickness of 0.125 mm and are modelled as a linear elastic material with a Young's modulus of 5.4 MPa (Watton et al. 2007). Following Watton et al. (2007), we assume that the valve leaflets possess a constant stiffness and uniform thickness and that the material exhibits a linear elastic response. These approximations were tested in earlier work, which found them to be acceptable for the physiological regime of interest (Watton et al. 2007). Each chord is attached at one end to the fixed points of the annular ring and at the other to one of two chordal attachment points that are fixed in space. The mitral annulus is fixed to a housing disc that is

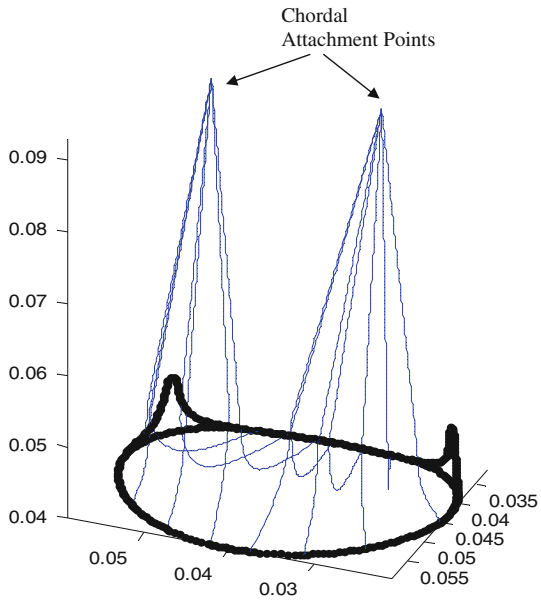

Fig. 5 The valve annulus and artificial chordae tendineae. The semi-rigid D-shaped annulus, shown in *black*, has a post height of 7.5 mm. The model chordae, which appear in *blue*, are comprised of a total of 1,802 fibre segments. Each chord is fixed at one end to the nearly rigid annular ring and at the other to one of two chordal attachment points (CAPs). In this study, these CAPs are fixed in space to facilitate comparison between simulation and experiment

mounted in a semi-rigid circular tube. All of these structures are immersed in a rectangular 16 cm × 8 cm × 8 cm fluid box; see Fig. 6.

In previous work using a formally second-order accurate cell-centred IB method (Griffith et al. 2009), we performed simulations using a version of this model that included a model of the bending stiffness of the chordae. In those simulations, we imposed motion of the chordal attachment points

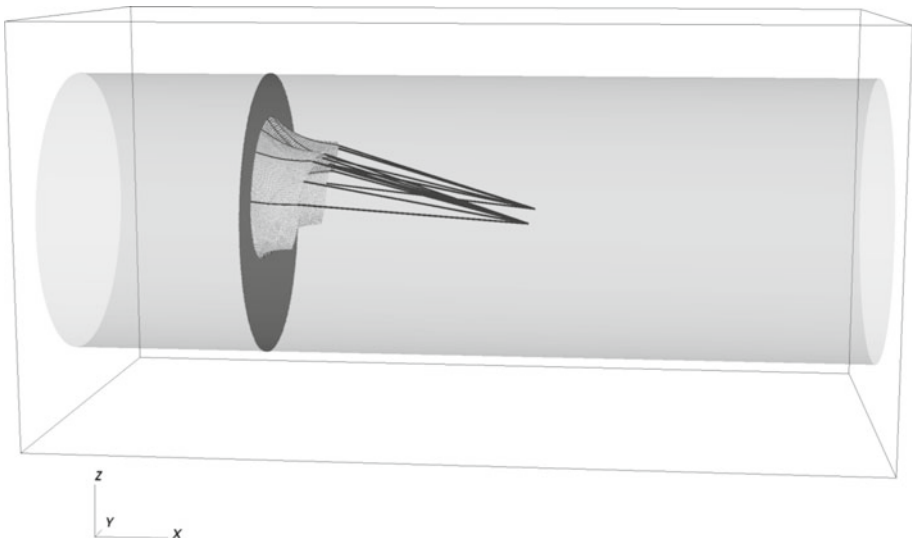

Fig. 6 The mitral valve and the housing disc mounted in a semi-rigid circular tube of length 16 cm and diameter 5.6 cm. The valve housing is placed 4 cm downstream of the inlet of the tube. These structure are embedded in a 16 cm × 8 cm × 8 cm fluid box. A time-dependent transvalvular pressure difference is imposed across the model valve by prescribing pressure boundary conditions at the inlet and outlet of the tube

that was derived from medical imaging data, and we prescribed the experimentally measured flow rate at the inlet of the tube along with zero-pressure boundary conditions at the outlet. We found that the peak pressure was significantly reduced in comparison to the peak pressures of earlier simulations that used a first-order accurate version of the IB method. Specifically, the transvalvular pressure difference required to open the valve was about 4 mm Hg, which compares favourably to the corresponding value of 12 mmHg obtained by Watton et al. (2007). We noted, however, that during the systolic phase of the cardiac cycle, the transvalvular pressure load was much smaller than the experimentally measured value. This is an important drawback of using flow rate as a boundary condition for these types of simulations: a realistic pressure load across a closed valve cannot be properly established.

In this study, we overcome this problem by imposing pressure boundary conditions at both the inlet and the outlet of the model. Specifically, we impose a pressure difference $dP(t)$ that is based on measurements obtained from flow experiments that used a prototype of the valve prosthesis. A schematic diagram of the experimental apparatus is shown in Fig. 7a; for a detailed description of this apparatus, see Fisher et al. (1986). The measured pressure difference $dP_{\text{exp}}(t)$ that we have available to use in our simulations was determined from two pressure transducers: one that was placed 2.5 cm upstream of the valve, identified as station U in Fig. 7a, and another that was placed 5 cm downstream of the valve, identified as station B in Fig. 7a. Notice, however, that we employ a flow chamber that is 16 cm long. This length was chosen to reduce the influence of the boundary conditions on the dynamics of the model. A consequence of this, however, is that we cannot use the experimental pressure measurements directly as boundary conditions for the model. Were we to do so, the simulated pressure difference in the model measured at stations U and B would generally be smaller than the experimentally measured difference in pressures at those locations. Moreover, the corresponding flow rates would also be smaller. Rather than using the experimental measurements directly as boundary conditions for our model, we instead set $dP(t) = dP_{\text{exp}}(t) + dP_{\text{shift}}(t)$, in which $dP_{\text{shift}}(t)$ is an additional driving pressure that is intended to offset the additional flow resistance presented by the longer flow chamber used in the simulations. The value of $dP_{\text{shift}}(t)$ was empirically determined so that the difference in the computed pressure between stations U and B is in good agreement with the experimental measurements, see Fig. 7b. Boundary conditions are also required for the portions of the fluid box that are exterior to the inlet and outlet of the flow chamber. Solid-wall boundary conditions are prescribed along the portions of the $x = 0$ cm and $x = 16$ cm boundaries that are exterior to the circular tube, and zero-pressure boundary conditions are imposed along the remainder of the domain boundary (Griffith et al. 2009).

Our simulations use a formally second-order accurate staggered-grid IB method (Griffith 2009, 2011a,b). The time step size was set to be $\Delta t = 1.25 \times 10^{-5}$ s, which was empirically determined to be approximately the largest stable time step size permitted by the model. Therefore, computing a complete 0.75 s cardiac cycle requires 6 million time steps, which required approximately 4 days on a Dell workstation (dual quad-core Intel Xeon X5450 3.0 GHz processors).

4.2 Results

To investigate the effect on valve dynamics of accounting for the bending stiffnesses of the leaflets, two simulations are carried out. In one simulation, we include the bending stiffnesses of the chordae but not of the valve leaflets; in the other simulation, we account for both chordal and leaflet

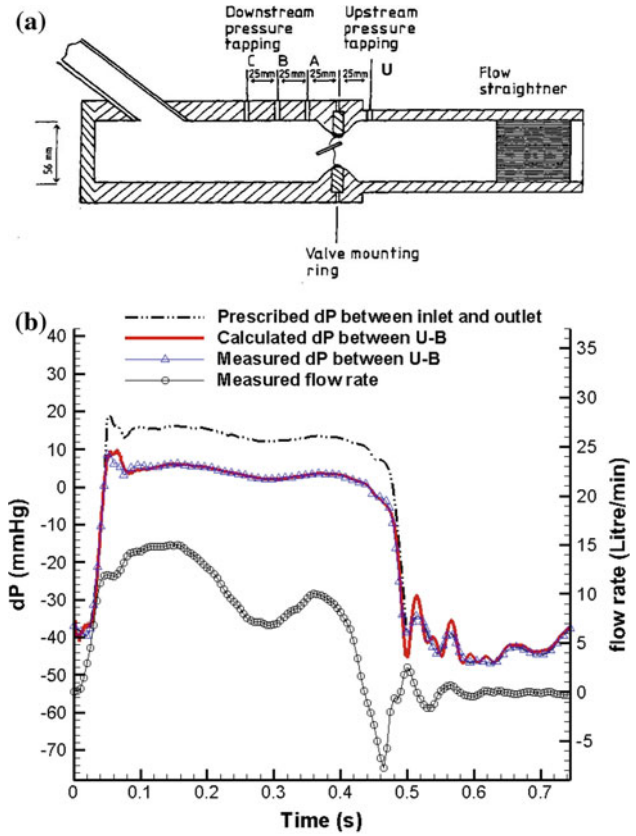

Fig. 7 **a** Schematic diagram of the experimental apparatus described by Fisher et al. (1986), in which flow is driven by a computer-controlled pump that generates pulsatile inflow. To avoid turbulence, the tubular Perspex section upstream from the valve is filled with straws that act as flow strengtheners. In the experiments, the flow volume was 80 ml per cycle, with a cycle duration of 0.75 s. The mean downstream pressure was 95 mmHg. The transvalvular pressure difference was measured between stations U and B. **b** The prescribed transvalvular pressure difference, which is imposed over the 16 cm tube (*dashdot*), and the computed pressure difference between stations U and B (*solid*) are compared to the experimentally recorded pressure difference (*solid with triangles*). The corresponding experimental flow rate is also shown (*solid with circles*)

bending stiffnesses. The simulated valve opening sequences, as viewed from the inlet boundary of the circular tube in which the valve is mounted, are shown in Fig. 8, panels (a) and (b). The corresponding experimental recordings are shown in Fig. 8c. Note that while the valve is open, the posterior chordae are clearly more taut than the anterior chordae. This is a consequence of the design of this mitral prosthesis. Specifically, the motion of the posterior leaflet is more constrained than that of the anterior leaflet. This phenomenon is observed both in the simulations and in corresponding experiments. This design defect also causes large strain and stress, as discussed in our previous studies (Watton et al. 2007, 2008).

Figure 8 clearly demonstrates that the best agreement between simulation and experiment is obtained when both the chordal and the leaflet bending stiffnesses are included in the model. In particular, the model that includes leaflet bending rigidity does not suffer from over-opening at the beginning of diastolic phase. When we neglect the bending stiffness of the leaflets, the leaflets are overly flexible, permitting the development of a much larger orifice in comparison to the experimental results. In fact, in this case, part of the anterior leaflet exceeds the boundary of the annulus. These results also suggest that chordal bending rigidity plays an important role in proper valve closure. The fact that the chordae exert forces that act to close the valve is clearly seen in Fig. 9. A similar phenomenon can also be seen in the experimental pictures around this time; see Fig. 8c.

The fluid pressure field generated by the model is shown in Fig. 10 at times when the valve is fully open and fully closed. The valve opens at a driving pressure difference of approximately 8 mmHg and is subject to a significant, physiological pressure load when closed. These loading conditions are substantially more realistic than those of our earlier simulations.

The flow rates yielded by the model with and without leaflet bending stiffnesses are shown in Fig. 11. It is interesting to see that if we only include the chordal stiffness, the computed flow rate is much larger than the experimental data, because the valve over-opens and yields an unrealistically *low* resistance to forward flow. Adding bending stiffnesses to the leaflets leads to a much closer agreement between simulation and experiments, including reduced oscillations in the flow record after valve closure.

The simulated and experimental effective valve orifice areas are plotted in Fig. 12. These quantities are estimated using the Gorlin formula (Gorlin and Gorlin 1951),

$$A = k\frac{Q}{\sqrt{dP_{UB}}} \tag{9}$$

in which A is the effective orifice area in cm^2, Q is the flow rate in litre/min, dP_{UB} is the difference in the pressure between stations U and B in mmHg, and $k = 1/(0.7*44.5*0.06)$ is an empirical constant (Rapaport 1985). It should be mentioned that the Gorlin formula is derived from a simplified description of fluid dynamics that can result in inaccuracies if the flow transients are strong, as occurs during valve opening and closure. We remark that the normal orifice area of a native mitral valve is 4–6 cm^2, whereas the estimated orifice area in both the experiment and in the simulation with leaflet bending forces is only about 2.5 cm^2, suggesting the need for further improvement to the current design.

5 Discussion and conclusion

In this study, we presented simulation results obtained via a fluid–structure interaction model of a chorded prosthetic

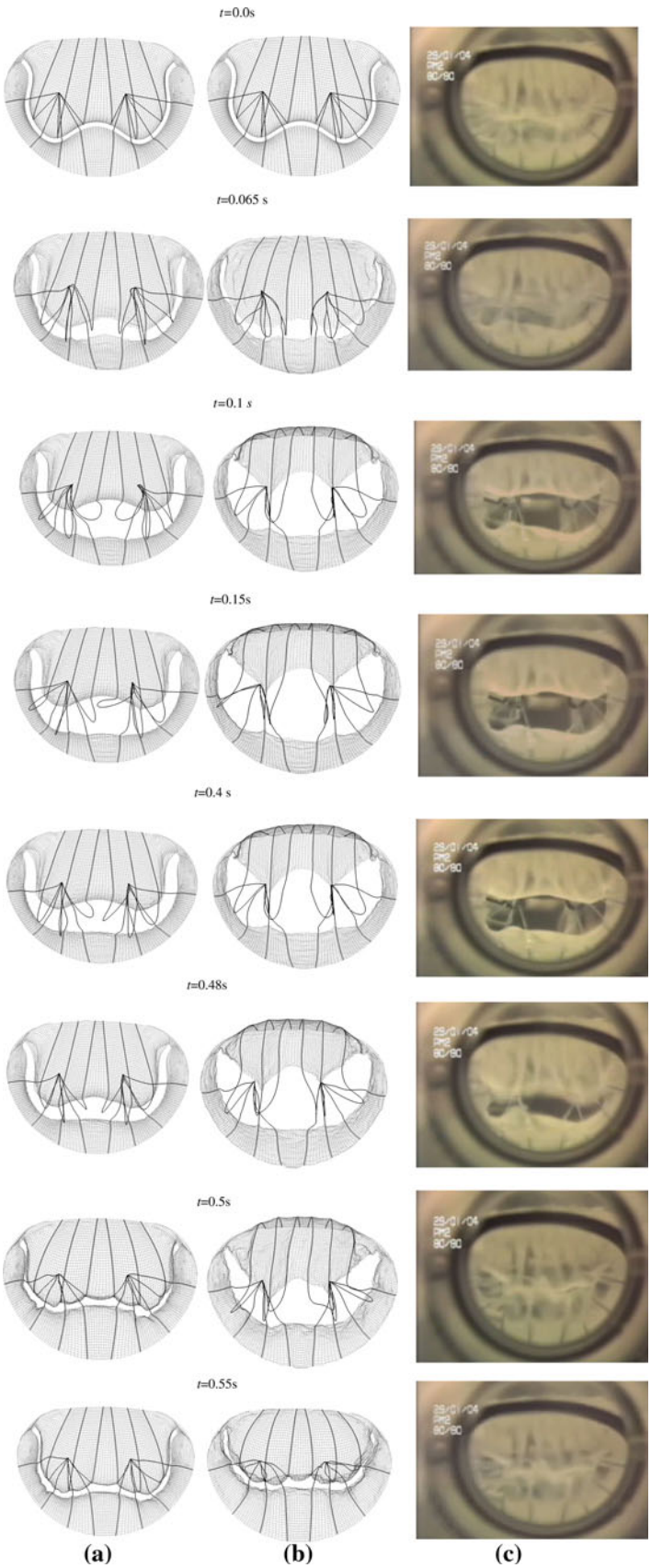

Fig. 8 View of the mitral valve from the inflow boundary during a complete cardiac cycle. **a** The model valve with both chordal and leaflet bending stiffnesses, **b** the model valve with only chordal bending stiffnesses and **c** the experimental recording. The bending stiffnesses of the chordae assist in valve closure; however, to prevent over-opening of the valve leaflets, it is necessary also to include leaflet bending stiffnesses in the model

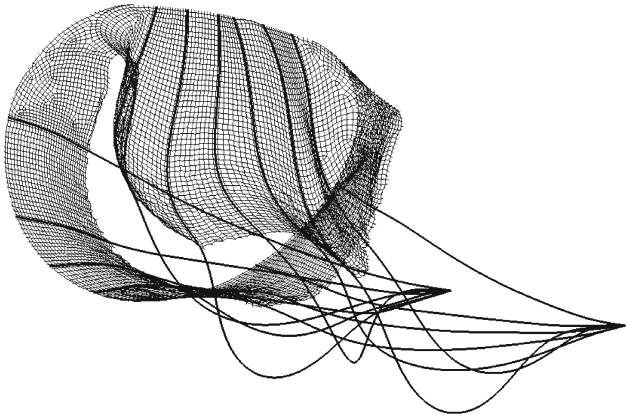

Fig. 9 View of a model mitral valve that includes both leaflet and chordal bending stiffnesses, showing that the chordae help to close the valve at $t = 0.4\,\mathrm{s}$

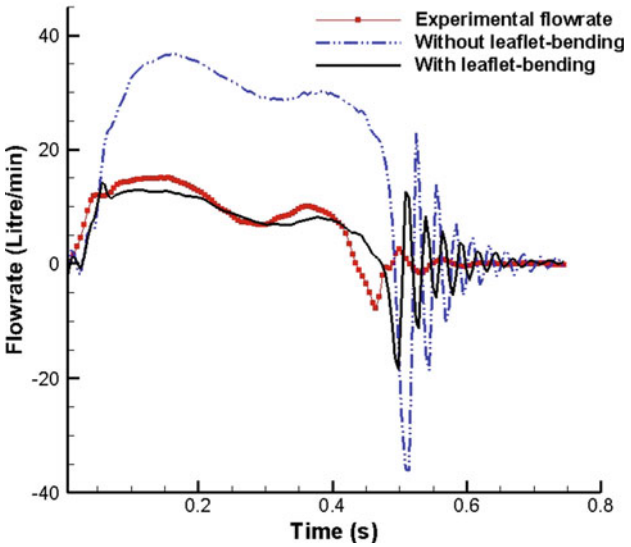

Fig. 11 Flow rates computed by the mitral valve models with and without leaflet bending stiffnesses, along with flow rates measured from the experimental test rig. Agreement between the model results and the experimental data is best when the model includes both chordal and leaflet bending stiffnesses

mitral valve, and we compared these results to measurements obtained from corresponding experiments using a real valve prosthesis. Our model accounted for both the chordal and leaflet bending stiffnesses, and it used a formally second-order accurate IB method. Previous simulations by this group using a first-order accurate IB method and periodic boundary conditions (Watton et al. 2007, 2008; Yin et al. 2010) suggested that the model mitral valve would not close unless additional pressure is added. This study shows that, by

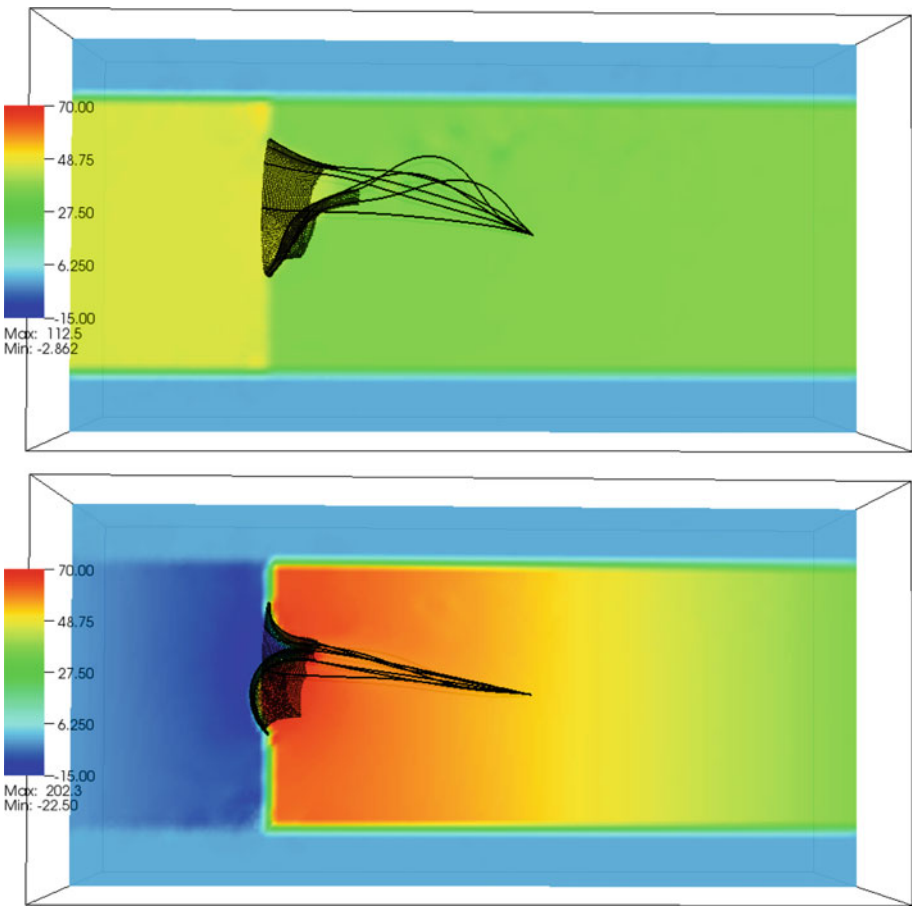

Fig. 10 The fluid pressure field along a plane bisecting the model valve shown when the mitral valve is fully open and fully closed. We remark that a realistic pressure load can be established when the valve is closed only by using pressure boundary conditions at both the inlet and the outlet of the model

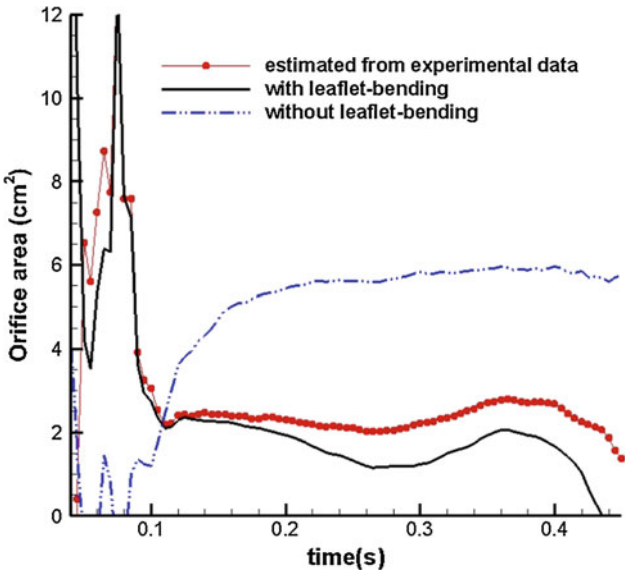

Fig. 12 Effective valve orifice area as a function of time during the opening phase, as determined by the Gorlin formula

including the chordal bending force in the model, the closure dynamics of the valve are improved significantly. Unless we include leaflet bending stiffness in our model, however, the valve leaflets remain overly flexible. Specifically, without such bending-resistant forces, the valve over-opens during the initial portion of the diastolic phase of the cardiac cycle, resulting in a valve orifice that is significantly larger than observed in corresponding experiments. Much better agreement in valve orifice size is achieved when we include the valve leaflet bending force. In addition, nonphysical oscillations that occur upon valve closure are greatly reduced when such forces are included in the model. These findings highlight the importance of accounting for the bending stiffness in the dynamic simulation of the mitral valve.

The current model has been improved from our previous mitral valve models (Watton et al. 2007, 2008; Griffith 2009; Yin et al. 2010) in several important aspects. Pressure boundary conditions are imposed, and the mechanical representation has been improved by accounting for the bending rigidity of the leaflets and the chordae. In addition, the model predictions are much closer to experimental data throughout the cardiac cycle, including both the opening and closing phases. We have also performed a quantitative verification of the IB method for a challenging problem in collapsible channel flow.

The present work also has several limitations. First, the mechanical structure of the mitral valve is modelled quite simply as a mesh of elastic fibres, and the bending stiffness is only provided along each fibre. This may contribute to the discrepancy between the predicted results and the experimental data, a discrepancy that is reduced but not eliminated in the present simulations, see Figs. 8 and 11. To better model the nonlinear mechanical behaviour of the mitral valve leaflets, it may be important to use a modelling approach that permits more sophisticated elasticity models. One approach, which we aim to pursue in future work, would be to employ a FE discretisation of the valve and to use experimentally characterised strain-energy functionals to describe the elasticity of the valve leaflets. Extensions of the IB method that permit such FE-based elasticity models have been developed over the past decade (Zhang et al. 2004; Boffi et al. 2008; Griffith and Luo 2011), and one such extension of the IB method is already implemented within the IBAMR software used to perform the simulations described herein (Griffith and Luo 2011). Second, although more realistic pressure boundary conditions are implemented in the present simulations, these boundary conditions do not include any feedback mechanisms that are able to adjust the flow and pressure resulting from compliances in the experimental setup. We believe that the lack of realistic compliance in the loading conditions is the principal reason for the oscillations seen after $t = 0.5$ s in our simulations. Future work on incorporating more realistic loading conditions is clearly required. Third, the annular ring in our model is assumed to be planar and fixed in space, whereas in case of a native valve, it is saddle shaped and deformable. In fact, in the real valve prosthesis, the annulus is rigid, and whereas the valve ring is not planar, accounting for this in the model may not be required to obtain realistic chordal force distributions and leaflet stresses (Prot et al. 2009). Finally, although the mitral valve is generally described as a passive structure, Prot and Skallerud (2009) found that their FE mitral valve model yields unrealistic deformations when the active muscle fibres of the anterior leaflet are neglected. A passive model of the mitral valve leaflets is appropriate in the present setting, in which we are modelling a passive polyurethane mitral valve prosthesis; however, the results of Prot and Skallerud suggest that our model may be of limited use if applied to interpret the behaviour of a native mitral valve.

In summary, we have successfully simulated the dynamic behaviour of a chorded mitral valve prosthesis and, in doing so, highlighted the importance of accounting for the bending stiffnesses of the leaflets and artificial chordae tendineae of the valve prosthesis. Although our observations are drawn from an IB model of the mitral valve that describes the elasticity of the valve in terms of systems of elastic fibres, we believe these findings would apply equally to structures with more traditional continuum-based descriptions. That is to say, we expect that a valve leaflet model that does not account for bending stiffnesses is unlikely to perform adequately in the dynamic setting. Therefore, constructing the realistic, dynamic models of native cardiac valves and valve prostheses that are needed to improve clinical outcomes for the large number of patients suffering from valvular heart diseases will require either a shell-type formulation, like that

used in the present work, or a fully three-dimensional description of the elasticity of the cardiac valves.

Acknowledgments This work is supported by the British Heart Foundation, by the Medical Research Scotland, and by the Excellence Exchange Project funded by the Xi'an Jiaotong University, China. B.E.G. also acknowledges research support from American Heart Association grant 10SDG4320049 and National Science Foundation grants DMS 1016554 and OCI 1047734.

References

Arnoldi A, Invernizzi A et al (2010) Mitral valve models reconstructor: a Python based GUI software in a HPC environment for patient-specific FEM structural analysis. Innov Adv Comput Sci Eng 215–219

Balay S, Eijkhout V et al (1997) Efficient management of parallelism in object oriented numerical software libraries. In: Arge E, Bruaset AM, Langtangen HP (eds) Modern software tools in scientific computing. Birkhäuser Press, Boston, pp 163–202

Balay S, Buschelman K et al (2008) PETSc users manual. Technical Report ANL-95/11—Revision 3.0.0, Argonne National Laboratory

Balay S, Buschelman K et al (2009) PETSc. Web Page: http://www.mcs.anl.gov/petsc

Boffi D, Gastaldi L et al (2008) On the hyper-elastic formulation of the immersed boundary method. Comput Methods Appl Mech Eng 197(25–28):2210–2231

Cai ZX, Luo XY (2003) A fluid-beam model for flow in a collapsible channel. J Fluids Struct 17(1):125–146

Dal Pan F, Donzella G et al (2005) Structural effects of an innovative surgical technique to repair heart valve defects. J Biomech 38(12):2460–2471

Einstein DR, Reinhall P et al (2003) Dynamic finite element implementation of nonlinear, anisotropic hyperelastic biological membranes. Comput Methods Biomech Biomed Eng 6(1):33–44

Einstein DR, Kunzelman KS et al (2005) Non-linear fluid-coupled computational model of the mitral valve. J Heart Valve Dis 14(3):376–385

Einstein DR, Del Pin F et al (2010) Fluid-structure interactions of the mitral valve and left heart: comprehensive strategies, past, present and future. Int J Numer Methods Biomed Eng 26(3–4):348–380

Falgout RD, Yang UM (2002) Hypre: a library of high performance preconditioners. In: Sloot PMA, Tan CJK, Dongarra JJ, Hoekstra AG (eds) Computational science—ICCS 2002 Part III, vol 2331, pp 632–641

Fisher J, Jack GR et al (1986) Design of a function test apparatus for prosthetic heart valves. Initial results in the mitral position. Clin Phys Physiol Meas 7:63

Gorlin R, Gorlin SG (1951) Hydraulic formula for calculation of the area of the stenotic mitral valve, other cardiac valves, and central circulatory shunts. I 1. Am Heart J 41(1):1–29

Griffith BE (2005) Simulating the blood-muscle-valve mechanics of the heart by an adaptive and parallel version of the immersed boundary method, PhD Thesis, Department of Mathematics, Courant Institute of Mathematical Sciences, New York University, New York

Griffith BE, Hornung RD et al (2007) An adaptive, formally second order accurate version of the immersed boundary method. J Comput Phys. 223(1): 10–49

Griffith BE (2009) An accurate and efficient method for the incompressible Navier–Stokes equations using the projection method as a preconditioner. J Comput Phys 228(20):7565–7595

Griffith BE (2011a) Immersed boundary model of aortic heart valve dynamics with physiological driving and loading conditions. Int J Numer Methods Biomed Eng (in press)

Griffith BE (2011b) On the volume conservation of the immersed boundary method. Commun Comput Phys (in press)

Griffith BE, Luo XY (2011) The immersed boundary method with finite element elasticity (submitted)

Griffith BE, Peskin CS (2005) On the order of accuracy of the immersed boundary method: higher order convergence rates for sufficiently smooth problems. J Comput Phys 208(1):75–105

Griffith BE, Luo XY et al (2009) Simulating the fluid dynamics of natural and prosthetic heart valves using the immersed boundary method. Int J Appl Mech 1(1):137–177

Hornung RD, Kohn SR (2002) Managing application complexity in the SAMRAI object-oriented framework. Concurr Comput Pract Experience 14(5):347–368

Hornung RD, Wissink AM et al (2006) Managing complex data and geometry in parallel structured AMR applications. Eng Comput 22(3–4):181–195

Kim HS (2009) Nonlinear multi-scale anisotropic material and structural models for prosthetic and native aortic heart valves. Georgia Institute of Technology

Kim H, Chandran KB et al (2007) An experimentally derived stress resultant shell model for heart valve dynamic simulations. Ann Biomed Eng 35(1):30–44

Kim H, Lu J et al (2008) Dynamic simulation of bioprosthetic heart valves using a stress resultant shell model. Ann Biomed Eng 36(2):262–275

Krishnamurthy G, Itoh A et al (2009) Stress-strain behavior of mitral valve leaflets in the beating ovine heart. J Biomech 42(12):1909–1916

Kunzelman KS, Cochran RP et al (1993) Finite-element analysis of mitral-valve pathology. J Long Term Eff Med Implants 3(3):161–170

Kunzelman KS, Reimink MS et al (1997) Annular dilatation increases stress in the mitral valve and delays coaptation: a finite element computer model. Cardiovasc Surg 5(4):427–434

Kunzelman KS, Quick DW et al (1998a) Altered collagen concentration in mitral valve leaflets: biochemical and finite element analysis. Ann Thorac Surg 66(6 Suppl):S198–S205

Kunzelman KS, Reimink MS et al (1998b) Flexible versus rigid ring annuloplasty for mitral valve annular dilatation: a finite element model. J Heart Valve Dis 7(1):108–116

Lai MC, Peskin CS (2000) An immersed boundary method with formal second-order accuracy and reduced numerical viscosity 1. J Comput Phys 160(2):705–719

Lim KH, Yeo JH et al (2005) Three-dimensional asymmetrical modeling of the mitral valve: a finite element study with dynamic boundaries. J Heart Valve Dis 14(3):386–392

Liu HF, Luo XY et al (2009) Sensitivity of unsteady collapsible channel flows to modelling assumptions. Commun Numer Methods Eng 25(5):483–504

Liu HF, Luo XY et al (2011) Stability and Energy budget of pressure-driven collapsible channel flows. J Fluid Mech (in press)

Luo XY, Cai ZX et al (2008) The cascade structure of linear instability in collapsible channel flows. J Fluid Mech 600:45–76

Maisano F, Redaelli A et al (2005) An annular prosthesis for the treatment of functional mitral regurgitation: Finite element model analysis of a dog bone-shaped ring prosthesis. Ann Thorac Surg 79(4):1268–1275

Peskin CS (2002) The immersed boundary method. Acta Numer 11:479–517

Prot V, Skallerud B (2009) Nonlinear solid finite element analysis of mitral valves with heterogeneous leaflet layers. Comput Mech 43(3):353–368

Prot V, Skallerud B et al (2007) Transversely isotropic membrane shells with application to mitral valve mechanics. Constitutive modelling and finite element implementation. Int J Numer Methods Eng 71(8):987–1008

Prot V, Haaverstad R et al (2009) Finite element analysis of the mitral apparatus: annulus shape effect and chordal force distribution. Biomech Model Mechanobiol 8(1):43–55

Prot V, Skallerud B et al (2010) On modelling and analysis of healthy and pathological human mitral valves: two case studies. J Mech Behav Biomed Mater 3(2):167–177

Rapaport E (1985) Calculation of valve areas. Eur Heart J 6(suppl C):21

Reimink MS, Kunzelman KS et al (1996) The effect of chordal replacement suture length on function and stresses in repaired mitral valves: a finite element study. J Heart Valve Di 5(4): 365–375

Sacks MS, Merryman DW et al (2009) On the biomechanics of heart valve function. J Biomech 42(12):1804–1824

Skallerud B, Prot V et al. (2011) Modeling active muscle contraction in mitral valve leaflets during systole: a first approach. Biomech Model Mechanobiol 10(1): 1–16

Stevanella M, Votta E et al (2009) Mitral valve finite element modeling: Implications of tissues' nonlinear response and annular motion. Journal of Biomechanical Engineering 131:121010

Urankar SA (2008) Modeling surgical interventions in the mitral valve with the finite element method. University of Pittsburgh, Pittsburgh

Vongpatanasin W, Hillis LD et al (1996) Prosthetic heart valves. N Engl J Med 335(6):407

Votta E, Maisano F et al (2007) The Geoform disease-specific annuloplasty system: a finite element study. Ann Thorac Surg 84(1):92–101

Votta E, Caiani E et al (2008) Mitral valve finite-element modelling from ultrasound data: a pilot study for a new approach to understand mitral function and clinical scenarios. Phil Trans R Soc A Math Phys Eng Sci 366:3411–3434

Watton PN, Luo XY et al (2007) Dynamic modelling of prosthetic chorded mitral valves using the immersed boundary method. J Biomech 40(3):613–626

Watton PN, Luo XY et al (2008) Effect of ventricle motion on the dynamic behaviour of chorded mitral valves. J Fluids Struct 24(1):58–74

Weinberg E (2005) Dynamic simulation of heart mitral valve with transversely isotropic material model. Massachusetts Institute of Technology

Weinberg EJ, Kaazempur-Mofrad MR (2007) A finite shell element for heart mitral valve leaflet mechanics, with large deformations and 3D constitutive material model. J Biomech 40(3):705–711

Weinberg EJ, Shahmirzadi D et al (2010) On the multiscale modeling of heart valve biomechanics in health and disease. Biomech Model Mechanobiol 9(4): 1–15

Wenk JF, Zhang Z et al (2010) First finite element model of the left ventricle with mitral valve: insights into ischemic mitral regurgitation. Ann Thorac Surg 89(5):1546–1553

Yin M, Luo XY et al (2010) Effects of flow vortex on a chorded mitral valve in the left ventricle. Int J Numer Methods Biomed Eng 26(3–4):381–404

Yoganathan AP, He Z et al (2004) Fluid mechanics of heart valves. Annu Rev Biomed Eng 6(1):331–362

Yoganathan AP, Chandran KB et al (2005) Flow in prosthetic heart valves: state-of-the-art and future directions. Ann Biomed Eng 33(12):1689–1694

Zhang L, Gerstenberger A et al (2004) Immersed finite element method. Comput Methods Appl Mech Eng 193(21–22):2051–2067